Theory for direct frequency-comb spectroscopy

Daniel Felinto and Carlos E. E. López
Departamento de Física, Universidade Federal de Pernambuco, 50670-901 Recife, PE, Brazil
(Received 3 May 2009; published 29 July 2009)

Direct frequency-comb spectroscopy is a technique that employs a train of well-stabilized ultrashort pulses to study the spectral properties of atomic or molecular systems. In this way, it opens the possibility of incorporating various coherent-control techniques for such spectral investigations. Here we introduce a theory for the interaction of a multilevel atom with such pulse trains, which is general enough to take into account an arbitrarily shaped frequency comb. We illustrate its application by studying the interaction of ^{87}Rb atoms with trains of pulses of various shapes, resonant with the 5*S*-5*D* two-photon transition of rubidium. More specifically, we treat the interaction with hyperbolic-secant pulses, chirped pulses, and 0-π pulses, respectively. The theory is designed to work at an arbitrary perturbation order. For the results presented here, we mostly used a 12th-order perturbation series at the pulse's electric field. Due to the large number of levels involved, such modeling may be quite complex computationally, and an important point of the present work is then to introduce the required numerical approach to treat this problem efficiently.

DOI: 10.1103/PhysRevA.80.013419 PACS number(s): 32.80.Qk, 82.53.Kp, 32.70.−n

I. INTRODUCTION

The recent development of well-stabilized frequency combs from femtosecond lasers has led to great advances in the field of metrology of optical frequencies [1,2]. In the first wave of applications of frequency combs to spectroscopy, the comb was employed as a mean to coherently connect atomic clocks directly to well-stabilized cw lasers, immediately leading to a considerable enhancement of precision for measurements performed with such lasers [1]. In this way, the frequency combs were perceived as the perfect complement for the already long tradition of high-resolution spectroscopy with cw lasers [3,4]. Direct frequency-comb spectroscopy (DFCS), however, is at the center of a second wave of applications of such combs to spectroscopy, one that takes advantage of this novel level of spectral control in a deeper way [5]. Here the comb as a whole is employed to probe the spectral properties of the medium. This has led to parallel high-resolution spectral analysis over large spectral regions [6,7], with possible applications to medicine due to the fast chemical analysis it enables [8]. Simultaneously, DFCS opens the way for applying coherent-control techniques to spectroscopy [5], a field still almost completely unexplored. Finally, it also enables high-resolution spectral analysis in regions of the spectrum that are difficult to reach with cw lasers, like in the extreme ultraviolet [9,10].

Even though it is quite recent the application of such frequency combs for ultra-high-resolution spectroscopy, and particularly for absolute frequency measurements with respect to atomic clocks, their possible use for spectroscopy was established already more than thirty years ago. In 1977, Teets *et al.* reported the first use of a train of light pulses to excite a two-photon atomic transition in sodium, producing spectral profiles with linewidths much smaller than the Fourier-transform limit of the individual pulses in the train [11]. Such narrow linewidths are a result of interference between the atomic excitation caused by consecutive pulses in the train, much like the interference responsible for the observation of Ramsey fringes [12]. The work by Teets *et al.* was followed by a series of proof-of-principle experiments demonstrating the adaptation of this idea to different spectroscopic techniques [13–19]. These first experiments, however, suffered from the difficulties in stabilizing the absolute phase between pulses of such pulse trains, rendering spectral information with considerably less resolution than what could be obtained with state-of-the-art stabilized cw lasers. This is the problem that was only recently solved, leading finally to spectra determined from pulse trains presenting already a resolution similar to the best cw-laser results reported in the literature [6].

The present work aims to introduce the necessary theoretical tools to model the excitation of multilevel atomic systems by an arbitrarily shaped frequency comb. In this way, we hope to contribute to the development of new spectroscopic tools merging coherent control, high resolution, and parallel excitation of multiple lines. The previous theoretical treatments for the interaction of trains of pulses with atomic systems were largely restricted to a small number of atomic levels and simple pulse shapes [20–28]. The theoretical treatment for multilevel atoms presented here is, in many ways, an extension of the one employed in Ref. [6] to treat the two-photon excitation of a cold rubidium sample by trains of ultrashort pulses. In the treatment of Ref. [6], however, the excitation was considered to be impulsive and the particular shape of the pulses was then completely disregarded. On the other hand, the excitation of atoms by trains of pulses with a complex shape has been investigated in other works both theoretical and experimentally [29–31]. The theoretical approach in those cases, however, was again restricted to a small number of levels, typically around three or four.

In the following, we are going to introduce the general theoretical framework for our work in Sec. II. Crucial aspects of the numerical implementation of this theory are explained in Sec. III. The treatment of these two sections are valid for a large class of atomic systems and pulse shapes. In order to illustrate its application, we employ it in Sec. IV to model the excitation of sequential, two-photon transitions in ^{87}Rb atoms by trains of ultrashort pulses of various pulse

shapes. We consider the fine and hyperfine structure of the relevant energy levels, resulting in a total of 16 atomic states involved in the process.

The general features of the coherent-accumulation process behind the spectral resolution of DFCS are discussed in Sec. IV A, still under the impulsive approximation employed in Ref. [6]. Differently from Ref. [6], however, we are able to work here at a considerably higher perturbation order, which effectively enables us to work with much higher pulse energies and to probe strongly saturated excitation regimes. We also discuss in Sec. IV A how to characterize the numerical errors in our program, and the present limitations of our numerical approach.

The calculations considering different pulse shapes are discussed in Secs. IV B–IV D. For the pulse shapes, we start by considering the usual hyperbolic-secant pulses (Sec. IV B) generated by femtosecond lasers, and then treat the cases of chirped pulses (Sec. IV C) and 0π pulses (Sec. IV D). In each of these sections, we analyze the main features of the spectrum that change with the pulse shape. Particularly interesting to illustrate the power of our method is the modeling of the excitation by 0π pulses, since the required spectral resolution in the calculation approaches here just a few comb lines. In this way, we emphasize that this method can be used to model the interaction of real atoms with frequency combs shaped at the level of a few frequency modes [32]. Finally, in Sec. V we discuss our conclusions for this work and the new perspectives it may open for the field.

II. GENERAL THEORY

Consider an electric field $E(t)$ interacting with a multilevel atom. The set of levels is denoted by $\{|i\rangle\}$. The Hamiltonian of the system is

$$\hat{H} = \hat{H}_0 + \hat{V}(t), \tag{1}$$

where

$$\hat{H}_0 = \sum_i E_i |i\rangle\langle i| \tag{2}$$

is the Hamiltonian for the free atom, with E_i being the energy of the ith level, and

$$\hat{V}(t) = -\sum_{i,j} V_{ij}(t)|i\rangle\langle j| + \text{H.c.} \tag{3}$$

is the interaction potential in the dipole approximation, with V_{ij} giving the time-dependent potential coefficient corresponding to transitions between levels i,j.

The Bloch equations for the time evolution of the system are then

$$\frac{\partial \rho_{ij}}{\partial t} = -\frac{i}{\hbar}\langle i|[\hat{H},\hat{\rho}]|j\rangle - \Gamma_{ij}\rho_{ij} + \delta_{ij}\sum_r \gamma_{ir}\rho_{rr}, \tag{4}$$

where Γ_{ij} stands for the relaxation rate of the ij component of the density matrix, δ_{ij} is the Kronecker delta function, and the term $\Sigma_r \gamma_{ir}\rho_{rr}$ gives the incoherent feeding of the ith level by the population of the upper r states.

Substituting the expression for the free-atom Hamiltonian, Eq. (4) can also be written as

$$\frac{\partial \rho_{ij}}{\partial t} = -(i\omega_{ij} + \Gamma_{ij})\rho_{ij} - \frac{i}{\hbar}\langle i|[\hat{V},\hat{\rho}]|j\rangle + \delta_{ij}\sum_r \gamma_{ir}\rho_{rr}, \tag{5}$$

where $\omega_{ij} = (E_i - E_j)/\hbar$ is the transition frequency between levels i,j.

Equation (5) can be integrated, resulting in the following integral equation:

$$\rho_{ij}(t)e^{(i\omega_{ij}+\Gamma_{ij})t} = \rho_{ij}^0 - \frac{i}{\hbar}\int_0^t dt' e^{(i\omega_{ij}+\Gamma_{ij})t'}\langle i|[\hat{V},\hat{\rho}]|j\rangle + \delta_{ij}\sum_r \gamma_{ir}\int_0^t dt' e^{\Gamma_{ii}t'}\rho_{rr}(t'), \tag{6}$$

with ρ_{ij}^0 giving the ρ_{ij} element at $t=0$.

We are interested in investigating the action of an ultrashort pulse over the atom. In this case, the interaction potential $\hat{V}$ is very fast compared to any relaxation time Γ_{ij}. The temporal dependence with Γ_{ij} can then be neglected inside the integrals that contain $\hat{V}$, and Eq. (6) becomes

$$\rho_{ij}(t) = e^{-(i\omega_{ij}+\Gamma_{ij})t}\left\{\rho_{ij}^0 - \frac{i}{\hbar}\int_0^t dt' e^{i\omega_{ij}t'}\langle i|[\hat{V},\hat{\rho}]|j\rangle + \delta_{ij}\sum_r \gamma_{ir}\int_0^t dt' e^{\Gamma_{ii}t'}\rho_{rr}(t')\right\}. \tag{7}$$

Since we want to follow the atomic temporal evolution with a long sequence of pulses, we need to obtain the expression that connects the state of the system prior to an arbitrary $(n+1)$th pulse to the state prior to the nth pulse. This expression is obtained from Eq. (7) by simply making $t=T_R$, where T_R is the laser repetition period. For the integrals that depends on $\hat{V}$, this is equivalent to make $t\to\infty$, since we are treating an ultrashort interaction. Equation (7) takes then the following form

$$\rho_{ij}^{n+1} = e^{-(i\omega_{ij}+\Gamma_{ij})T_R}(\rho_{ij}^c + \delta_{ij}I_i), \tag{8}$$

where

$$\rho_{ij}^c = \rho_{ij}^n - \frac{i}{\hbar}\int_0^\infty dt' e^{i\omega_{ij}t'}\langle i|[\hat{V}^n(t),\hat{\rho}^c]|j\rangle \tag{9}$$

gives the state of the system $\hat{\rho}^c$ impulsively excited by the nth pulse ($\hat{V}^n$) starting from the state $\hat{\rho}^n$ prior to that pulse, and

$$I_i = \sum_r \gamma_{ir}\int_0^{T_R} dt' e^{\Gamma_{ii}t'}\rho_{rr}(t'). \tag{10}$$

Equation (8) states in a clear way that the overall evolution of the atomic state, when excited by a train of ultrashort pulses, is a combination of an impulsive excitation by the electric field followed by the incoherent redistribution of population among the various states caused by spontaneous emission. These two effects develop in very different timescales, which effectively allows us to decouple them and

separately evaluate their contributions, as described in the following two subsections.

A. Coherent excitation

In order to evaluate the ρ_{ij}^{c} terms, it is important to rewrite Eq. (9) in a way that is more suitable for calculations, as a function of the temporal evolution operator in the interaction picture $\hat{U}_I^n$. This operator can be written as a Dyson series in the form

$$\hat{U}_I^n = 1 + \left(-\frac{i}{\hbar}\right)\int_0^\infty dt' \hat{V}_I^n(t') + \left(-\frac{i}{\hbar}\right)^2 \int_0^\infty dt' \int_0^{t'} dt'' \hat{V}_I^n(t')\hat{V}_I^n(t'') + \cdots, \quad (11)$$

where

$$\hat{V}_I^n(t) = e^{i\hat{H}_0 t/\hbar}\hat{V}^n(t)e^{-i\hat{H}_0 t/\hbar} \quad (12)$$

gives the interaction potential in the interaction picture. As a function of $\hat{U}_I^n$, the integral equation (9) becomes then

$$\rho_{ij}^{c} = \langle i|\hat{U}_I^n \rho^n \hat{U}_I^{n\dagger}|j\rangle = \sum_{k,l} \rho_{k,l}^n \langle i|\hat{U}_I^n|k\rangle\langle l|\hat{U}_I^{n\dagger}|j\rangle. \quad (13)$$

In the form (13), ρ_{ij}^{c} is then obtained from the initial-state components ρ_{kl}^n and the complex transition matrix

$$U_{ij}^n = \langle i|\hat{U}_I^n|j\rangle, \quad (14)$$

which can be calculated directly from the expansion (11), particularly useful for obtaining perturbative solutions.

1. Pulse train

The calculation of the time evolution operator for the nth pulse in the train is simplified once we remember that, for a well-stabilized frequency comb [1,2], its electric field is given by

$$E_n(t) = E_0(t - nT_R)e^{2\pi nif_0 T_R} \quad (15)$$

with $E_0(t)$ the electric field for the first pulse in the train, T_R the laser repetition period, and f_0 the offset frequency of the comb [2]. We are also writing the electric field for the first pulse as $E_0(t)=\mathcal{E}(t)e^{i\omega_L t}$, where $\mathcal{E}(t)$ is the pulse envelope and ω_L the laser center frequency. When we treat the action of well-stabilized frequency combs, we are essentially discussing a pulse train with well stabilized f_0 and $f_R=1/T_R$, the laser repetition frequency. An essential point for the recent development of high-resolution spectroscopy with frequency combs is exactly that f_0 and f_R can be directly phase locked to any frequency standard, like a cesium atomic clock [1,2]. Defining f_0 in the way of Eq. (15), we have that each comb mode can be identified by an integer N, such that its frequency is

$$\nu_N = Nf_R - f_0. \quad (16)$$

With Eq. (15) in mind and using already the rotating-wave approximation, the interaction potential for the electric-dipole interaction of the nth pulse with the atom can be written as

$$\hat{V}^n(t) = \sum_{i,j} \mu_{i,j} E_0(t - nT_R)e^{2\pi nif_0}|i\rangle\langle j| + \text{H.c.}, \quad (17)$$

with $\mu_{i,j}$ the electric dipole moment for the transition $i \to j$, and the indices i,j running over all states in the system, with $j>i$. This ordering helps to clarify that all transitions to lower energies are acted by fields with a phase factor of $e^{2\pi nif_0}$ per transition. With this in mind, we have the following expression for the time evolution operator for the nth pulse $\hat{U}_I^n$ as a function of the one for the first pulse $\hat{U}_I^0$,

$$\hat{U}_I^n = \Phi_n \hat{U}_I^0 \Phi_n^\dagger, \quad (18)$$

where Φ_n is a diagonal matrix with the same dimensions as $\hat{U}_I^0$, and with its elements given by

(i) δ_{jk}, for states j in the first manifold of states of lowest energy;

(ii) $e^{2\pi nif_0 T_R}\ \delta_{jk}$, for states j in the second manifold of states, i.e., the manifold containing all states connected to the first manifold by a single electric-dipole transition;

(iii) $e^{2\pi nMif_0 T_R}\ \delta_{jk}$, for states j in the $(M+1)$th manifold of states, i.e., the manifold containing all states connected to the Mth manifold by a single electric-dipole transition, and of higher energies than the states of the Mth manifold.

The state ordering assumed above ensures that the Mth manifold have increasing energies as M is increased. Note that to prove Eq. (18), one just have to show that it is valid when we substitute $\hat{U}_I$ by $\hat{V}_I$.

B. Incoherent redistribution

The incoherent redistribution of population is described by the second term on the right side of Eq. (8). This term can be calculated in a straightforward way by expanding it in a series representing the cascade decay by spontaneous emission starting from the highest-energy level, and using the fact that this incoherent redistribution occurs in a much longer timescale than the coherent excitation by the ultrashort pulse. In this way, we can write

$$\begin{aligned} I_i &\approx \sum_r \gamma_{ir}\rho_{rr}^{c}\int_0^{T_R} dt' e^{(\Gamma_{ii}-\Gamma_{rr})t'} \\ &\quad + \sum_{r,s} \gamma_{ir}\gamma_{rs}\int_0^{T_R} dt' e^{(\Gamma_{ii}-\Gamma_{rr})t'}\int_0^{t'} dt' e^{(\Gamma_{rr}-\Gamma_{ss})t''}\rho_{ss}(t'') \\ &\approx \sum_r \gamma_{ir}\rho_{rr}^{c}\int_0^{T_R} dt' e^{(\Gamma_{ii}-\Gamma_{rr})t'} \\ &\quad + \sum_{r,s} \gamma_{ir}\gamma_{rs}\rho_{ss}^{c}\int_0^{T_R} dt' e^{(\Gamma_{ii}-\Gamma_{rr})t'}\int_0^{t'} dt' e^{(\Gamma_{rr}-\Gamma_{ss})t''} + \cdots. \end{aligned} \quad (19)$$

In the above series, the first term gives the redistribution coming from just one spontaneous emission event, connecting levels separated by just one dipole-allowed transition. The second term comes from a cascade of two spontaneous

emissions, connecting levels separated by two dipole allowed transitions in a cascade configuration. The series continues then until describing the decay cascade starting from the highest-energy level included in the model.

In terms of the dipole moments $\mu_{i,j}$, the various $\gamma_{i,j}$ are given by

$$\gamma_{i,j} = \frac{|\mu_{i,j}|^2}{\Sigma_k |\mu_{k,j}|^2} \Gamma_{jj}, \tag{20}$$

with k running over all states to which the jth state can decay.

C. Impulsive approximation

An interesting parameter to characterize the action of a pulse over the atom is what we call "atomic pulse area"

$$\theta_a = \frac{2ea_0}{\hbar} \int_{-\infty}^{\infty} \mathcal{E}(t) dt, \tag{21}$$

with e the electric charge and a_0 the Bohr radius. For a pulse that is very short when compared to the timescales determined by the detunings to any atomic transition, note that we can approximate

$$\frac{1}{\hbar} \int_{-\infty}^{\infty} \hat{V}_I^0(t) dt \approx \frac{\theta_a}{2} \hat{M}, \tag{22}$$

with $\hat{M}$ a matrix of the normalized dipole moments of the transitions $\hat{M}_{ij} = \mu'_{i,j}$, and $\mu'_{i,j} = \mu_{i,j}/ea_0$. If, besides being very short, its pulse envelope $\mathcal{E}(t)$ could be describe by a real function, note that we would also have

$$\int_{-\infty}^{\infty} dt_1 \int_{-\infty}^{t_1} dt_2 \cdots \int_{-\infty}^{t_{n-1}} dt_n \mathcal{E}(t_1)\mathcal{E}(t_2)\cdots\mathcal{E}(t_n) = \frac{1}{n!}\left[\int_{-\infty}^{\infty} \mathcal{E}(t) dt\right]^n. \tag{23}$$

In this case, the time evolution operator can be approximated by

$$\hat{U}_I^0 \approx 1 + \left(-\frac{i\theta_a}{2}\right)\hat{M} + \left(-\frac{i\theta_a}{2}\right)^2 \frac{\hat{M}^2}{2!} + \cdots, \tag{24}$$

or just

$$\hat{U}_I^0 \approx e^{-i\theta_a \hat{M}/2}. \tag{25}$$

This simplified expression can be very useful to model some physical situations or to obtain first, approximate solutions for more complex problems. An example of successful application of this approximation can be found in Ref. [6], where spectrally broad, approximately hyperbolic-secant pulses were employed to probe the $5S \rightarrow 5P \rightarrow 5D$ transition in an ensemble of laser-cooled rubidium atoms. It could not be applied, however, to model situations where the pulse shape plays a significant role, as in the case of the 0π pulses of Ref. [29] and the frequency-chirped pulses of Ref. [30].

D. Spectral-mask resolution

A frequency comb represents a collection of hundreds of thousands phase-locked frequency modes. Since we aim at modeling the action of an arbitrarily shaped frequency comb, it is important to determine the maximum spectral resolution achieved by the present theory. Our main limitation comes from the requirement of the whole pulse being much shorter than the laser repetition period T_R. This requirement is introduced to obtain the approximated Eq. (19).

Since $1/T_R$ gives the separation between consecutive comb modes, the spectral resolution $\Delta\nu_{res}$ for our theory should be then $\Delta\nu_{res} \gg 1/T_R$, or a number $N_{res} \gg 1$ of frequency modes. In this way, the present theory should work to model pulses modified by spectral masks with resolution equivalent, roughly, to a number of modes N_{res} such that

$$1 \text{ million} > N_{res} \gtrsim 10.$$

This resolution is enough to model a large class of spectral masks. For spectral resolutions equivalent to $N \lesssim 10$ the present theory will still produce consistent solutions, in the sense that the temporal evolution of the system will preserve the normalization of the density matrix describing the system. The results, however, should be regarded as approximations to the solution whose validity decreases as N_{res} approaches unity.

III. NUMERICAL APPROACH

From the previous section, we notice that the hard part of the problem is to calculate $\hat{U}_I^0$ for a particular problem. Once we have that, we can directly calculate $\hat{U}_I^n$ with Eq. (18). With $\hat{U}_I^n$ and the expression for I_i, its straightforward to obtain $\hat{\rho}^{n+1}$ from $\hat{\rho}^n$, Eq. (8). In this way, we can model the time evolution of $\hat{\rho}(t)$ from an initial state $\hat{\rho}^0$ up to an arbitrary number of periods of the exciting laser.

However, besides the case of an impulsive excitation (Sec. II C), to find an expression for $\hat{U}_I^0$ means to numerically compute the Dyson series, Eq. (11), up to a certain perturbation order m, i.e., up to a term with mth order integrals. At first sight, it may seem that this problem becomes rapidly hopeless as the perturbation order increases. Fortunately, this is not the case. Since we are dealing with a specific kind of mth order integral, time propagators, we can actually numerically compute the Dyson series up to any perturbation order as if it was a order-one integral, with the computational time increasing linearly with m.

To understand this crucial point, consider first an electric field defined by a long vector, size N, specifying its envelope values $\mathcal{E}_i$ at times t_i. Note that this is the most general situation when we consider the action of an arbitrarily shaped pulse over atomic systems. Usually, we have a nicely shaped hyperbolic-secant pulse at the laser output, which then passes through a series of elements to modify its shape in an arbitrary way. These elements can be a simple transparent medium, a vapor cell at room temperature, a grating pair with a liquid crystal mask in the middle [33–35], etc. Their action over the pulse shape can be well modeled by transfer functions in frequency space. The result of their action, however,

does not usually result in an analytical function in time. In this case, we are compelled to describe the pulse electric field in time by the discrete set of values $\mathcal{E}_i$ numerically calculated through the inverse fast Fourier transform of its modified expression in frequency space.

Consider now a set of matrices $\hat{P}_j$, with j going from 0 to m, of the same dimension as $\hat{V}_I^0$. At time t_0, much before the pulse arrived, we would have

$$\hat{P}_0(t_0) = \mathbf{1}, \tag{26a}$$

$$\hat{P}_1(t_0) = \mathbf{0}, \tag{26b}$$

$$\hat{P}_2(t_0) = \mathbf{0}, \tag{26c}$$

$$\vdots \tag{26d}$$

$$\hat{P}_m(t_0) = \mathbf{0}, \tag{26e}$$

with 1 the identity matrix and $\mathbf{0}$ a matrix of zeros only. At any later time t_i, these matrices would become

$$\hat{P}_0(t_i) = \mathbf{1}, \tag{27a}$$

$$\hat{P}_1(t_i) = \hat{P}_1(t_{i-1}) - \frac{i\Delta t}{\hbar}\hat{V}_I^0(t_i)\hat{P}_0(t_i), \tag{27b}$$

$$\hat{P}_2(t_i) = \hat{P}_2(t_{i-1}) - \frac{i\Delta t}{\hbar}\hat{V}_I^0(t_i)\hat{P}_1(t_i), \tag{27c}$$

$$\vdots \tag{27d}$$

$$\hat{P}_m(t_i) = \hat{P}_m(t_{i-1}) - \frac{i\Delta t}{\hbar}\hat{V}_I^0(t_i)\hat{P}_{m-1}(t_i). \tag{27e}$$

In the expressions above Δt is the time interval between two consecutive t_i's. Note that, by using a small enough Δt and calculating the $\hat{P}_j$'s from t_0 to time t_N, we are able to approximate

$$\hat{U}_I^0 \approx \hat{P}_0(t_N) + \hat{P}_1(t_N) + \hat{P}_2(t_N) + \cdots + \hat{P}_m(t_N), \tag{28}$$

up to the mth perturbation order.

The calculation represented by Eqs. (27) corresponds to the application of the rectangular rule for numerical integrations [36]. It provides the most straightforward numerical algorithm connecting the theory of Sec. II to a final program implementing such calculation. However, as usual for such integration problems, a considerably better algorithm, with respect to precision and efficiency, is obtained by the application of the trapezoidal rule instead [36]. In this case, Eqs. (27) are modified to

$$\hat{P}_0(t_i) = \mathbf{1}, \tag{29a}$$

$$\hat{P}_1(t_i) = \hat{P}_1(t_{i-1}) - \frac{i\Delta t}{2\hbar}[\hat{V}_I^0(t_i)\hat{P}_0(t_i) + \hat{V}_I^0(t_{i-1})\hat{P}_0(t_{i-1})], \tag{29b}$$

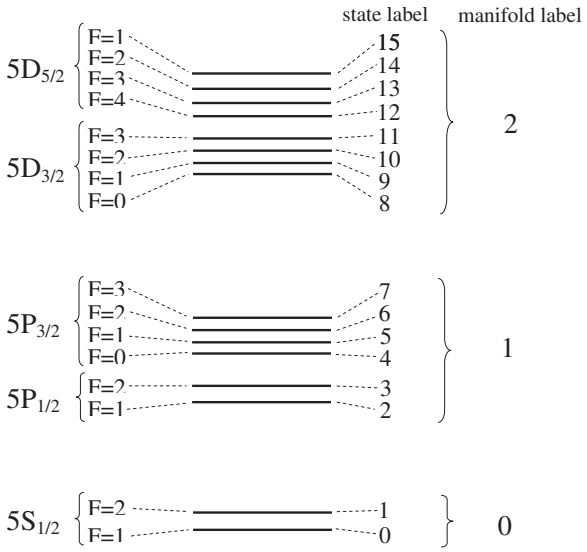

FIG. 1. Energy levels. On the left, the quantum numbers specifying each level. On the right, the respective state and manifold labels assigned in the various programs.

$$\hat{P}_2(t_i) = \hat{P}_2(t_{i-1}) - \frac{i\Delta t}{2\hbar}[\hat{V}_I^0(t_i)\hat{P}_1(t_i) + \hat{V}_I^0(t_{i-1})\hat{P}_1(t_{i-1})], \tag{29c}$$

$$\vdots \tag{29d}$$

$$\hat{P}_m(t_i) = \hat{P}_m(t_{i-1}) - \frac{i\Delta t}{2\hbar}[\hat{V}_I^0(t_i)\hat{P}_{m-1}(t_i) + \hat{V}_I^0(t_{i-1})\hat{P}_{m-1}(t_{i-1})]. \tag{29e}$$

In the following, all programs are setup using Eqs. (29). In this way, we can calculate $\hat{U}_I^0$ by running just once over the times t_i for an arbitrary perturbation order m. The computer memory needed is the one to store the long vector specifying the electric field, and two complete sets of $\hat{P}$ matrices (for times t_i and t_{i-1}), which are modified at every step of the above calculation. As can be seen from Eqs. (29), if we increase the perturbation order m by a number q we just add q new equations to that set, effectively increasing linearly the required computational time.

IV. APPLICATION TO ^{87}Rb

As a first application of our model, consider the excitation of the transition $5S \rightarrow 5P \rightarrow 5D$ of ^{87}Rb by a train of femtosecond laser pulses. This transition involves 16 hyperfine states, see Fig. 1, distributed over three manifolds. The first manifold, labeled 0, contains the two hyperfine states of level $5S_{1/2}$. The second, intermediate manifold is labeled 1, and includes the two hyperfine states of level $5P_{1/2}$ and the four states of level $5P_{3/2}$. The transitions from manifold 0 to 1 include then all D_1 and D_2 lines of ^{87}Rb, at 795 and 780 nm, respectively. The third, highest manifold is labeled 2, and includes the eight hyperfine states of levels $5D_{3/2}$ and $5D_{5/2}$. The laser is tuned to have its central wavelength resonant to the $5S \rightarrow 5D$ two-photon transition, at 778 nm. The manifold

label is used to calculate the Φ_n matrix in Eq. (18). The individual states are each labeled also with a number from 0 to 15, for increasing state energies.

The dipole moments between states i and j, $\mu_{i,j}$, are calculated as an average over all allowed π transitions (connecting states with the same magnetic quantum number m_F). In this way, we are treating the case of linearly polarized laser fields exciting atoms at zero magnetic field, as in Ref. [6]. The dipole moments are stored in a $\hat{M}$ matrix, in their normalized version $\mu'_{i,j}$, as defined in Sec. II C.

The intensity of the electric fields will be always given in terms of the "atomic pulse area" θ_a (Sec. II C) for the pulses at the laser output, considering them as hyperbolic-secant pulses at that point. This means that, when implementing the theory of Sec. II, we will make the substitution

$$\frac{\mu_{i,j}\mathcal{E}(t)}{\hbar} \rightarrow \frac{\mu'_{i,j}\theta_a}{2}\mathcal{E}'(t),$$

with $\mathcal{E}'(t)$ a function giving the temporal shape of the pulse. In general, the function $\mathcal{E}'(t)$ is obtained from the application of a transfer function (in frequency space) over an original hyperbolic-secant pulse with unit area for the field envelope. This notation facilitates the transition from the impulsive theory of Sec. II C to the general theory with arbitrary pulse shapes. It also provides a more intuitive measure of the pulse strength. A pulse with $\theta_a \approx \pi$, for example, indicates an intense pulse capable of nearly invert a single-photon transition, if applied to the sample right at the laser output. Pulses with $\theta_a \ll \pi$, on the other hand, are very weak, leading to small populations on the excited states. Note that the actual area of the pulse acting on the atoms will depend on θ_a multiplied by the area of the envelope $\mathcal{E}'(t)$, after its distortion by an arbitrary transfer function. A 0π pulse, for example, would have such area equal to zero (see Ref. [37]) even though the pulses would have a finite atomic area θ_a at the laser output.

The study of this particular set of atomic transitions, Fig. 1, is also convenient because the frequency of the corresponding states were all measured with great precision by various investigations employing cw lasers [38–40]. These measurements provide then independent inputs for the calculations, which can be compared to the experiments performed with frequency combs [6]. Also, the population of level $5D$ can be observed in this system through its decay to level $6P$ and then back to level $5S$, with emission of light at 420 nm (blue), a very different wavelength when compared to the laser's 778 nm (infrared) required for the two-photon transition $5S \rightarrow 5P \rightarrow 5D$. This is a standard procedure employed in various works [6,19,29]. Due to this possibility, the main quantity we calculate and plot in the following is the $5D$ population, the sum of all populations in manifold 2, without distinguishing which particular state it comes from.

In the following, we will start in Sec. IV A by describing the general features of the coherent-accumulation process [41–43] behind the high resolution of the DFCS technique. For this, we will employ the simple impulsive approximation, which is enough to explain all the basic features of the problem. Similar analysis can also be found in Refs. [6,44], which also uses the impulsive approximation, up to the fourth order in θ_a. It is provided again here, briefly, for completeness and to help the understanding of the other sections. On the other hand since our theory here is setup to work at arbitrary perturbation order, we were able to work here at a considerably higher order (12th) than in these previous references. In this way, our work could be extended well into the nonlinear region of interaction between atom and pulse train.

In Sec. IV B we finally start to model pulses with an arbitrary temporal profile by considering the simplest case of hyperbolic-secant pulses. We investigate then the effect of their temporal width T_p by calculating the spectra obtained with pulses of $T_p = 10$ fs and 100 fs, respectively. In Sec. IV C we consider the excitation by hyperbolic-secant pulses with some frequency chirp. This is the simplest modification a femtosecond laser pulse can go through since it can be introduced during its propagation through simple optical elements or even a piece of glass. The 0π pulses explored in Sec. IV D, on the other hand, require a more sophisticated spectral mask: a heated vapor cell with atoms resonant to the laser pulse. In this case, we are typically interested in modeling how such pulses, distorted by the propagation through the vapor cell, would interact with a second atomic sample consisting of cold atoms obtained, for example, from a magneto-optical trap.

A. Impulsive approximation

As anticipated above, most of the basic features of the coherent-accumulation process behind DFCS can be explained still under the impulsive approximation of Sec. II C. It provides also a reasonable, simple model to various experiments, as demonstrated in Refs. [6,44]. For these reasons, we will start our discussion by exploring the modeling of the system under this approximation.

After an ultrashort pulse excites an atom initially in its ground state (manifold 0), the excited atomic coherences and populations start to decay freely. In this process, various atomic coherences precess rapidly, with frequencies in the optical region. When the next pulse in the train arrives, it carries a fixed relative phase ($2\pi f_0 T_R$ in the rotating-wave approximation) with respect to the previous pulse, and finds the slowly varying coherences also at an arbitrary phase determined by their free evolution. If this interpulse phase plus the coherence phase of a particular atomic transition results in a multiple of 2π, we observe a constructive interference of the atomic excitation related to that transition. An example of such constructive interference can be found in the solid line of Fig. 2, where we tuned f_0 and f_R so that two teeth of the frequency comb would be resonant to the sequential transition $1 \rightarrow 7 \rightarrow 12$, with these numbers representing the state labels shown in Fig. 1. In this case, we considered $f_0 = 10$ MHz and $f_R = f_{ref} + \Delta f_R$, with $f_{ref} = 100$ MHz and $\Delta f_R = 6.8198$ Hz. Note that the laser period is around 10 ns, so that at 3 μs the atom interacted already with 300 pulses. To be precise, it is important to have in mind that the complete atomic population as a function of time should reveal a series of spikes and decays, repeated at every period T_R of the train

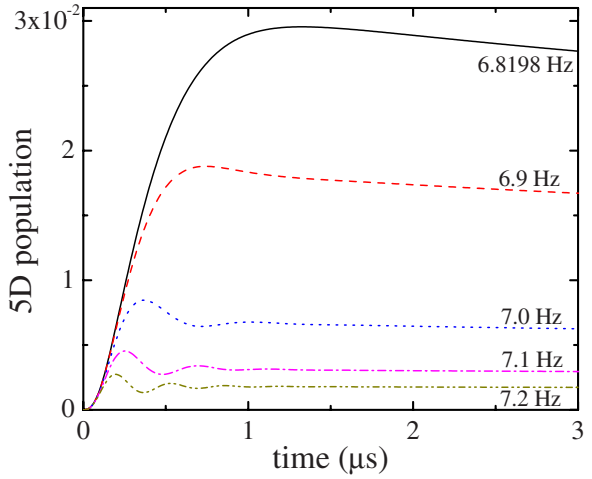

FIG. 2. (Color online) Time variation of the $5D$ population as the atom is excited by the pulse train. From the highest to the lowest curve, we have Δf_R=6.8198, 6.9, 7.0, 7.1, and 7.2 Hz, respectively. For these curves, we also have f_0=10 MHz, f_{ref}=100 MHz, and θ_a=0.01π.

[29]. The kind of theory presented here, on the other hand, provides the smooth curve marking the lowest point of this oscillatory behavior, which is proportional to the average population during a particular period of the process, as discussed in detail in Ref. [29].

Once we change Δf_R slightly, we see in Fig. 2 that the resonance condition is progressively lost. The excitations from different pulses do not add up coherently anymore, and the resulting $5D$ population decreases. Of course, as the interpulse phase difference, with respect to resonance, is increased, the excited $5D$ population deviates more rapidly from the one expected at resonance. This observation is actually better presented in Fig. 3, where we plot the $5D$ population after different numbers of pulses as the detuning from resonance is modified.

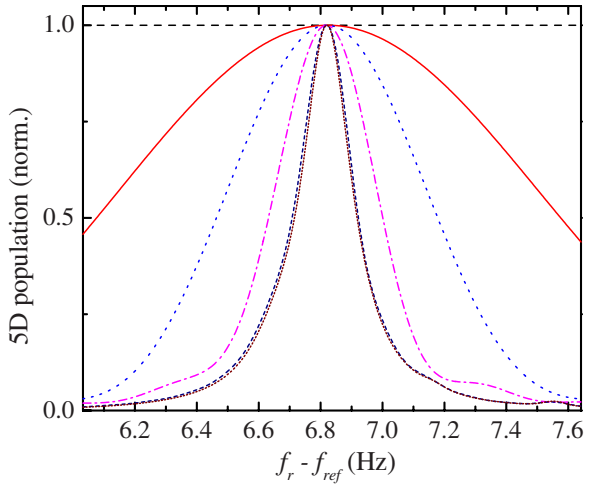

FIG. 3. (Color online) Normalized $5D$ population as a function of the detuning from an atomic resonance, for trains of pulses composed of different numbers of pulses. The dashed line represents the excitation by a single pulse. The other lines, from the largest to the smallest linewidth, represent pulse trains with 10, 20, 40, 100, and 200 pulses, respectively. All other parameters are the same as in Fig. 2.

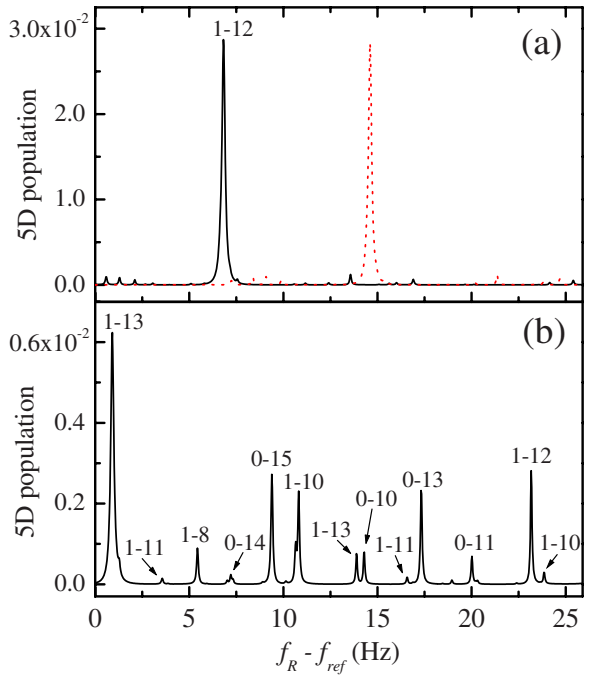

FIG. 4. (Color online) Population in level $5D$ as a function of f_R for (a) f_{ref}=100 MHz and (b) f_{ref}=100.12 MHz. The solid lines are obtained with f_0=10 MHz. The dashed line in (a) is obtained with f_0=40 MHz. The labels $(i-j)$ in each peak indicate the initial (i) and final (j) states of each two-photon resonance. The atomic pulse area is here θ_a=0.01π, and we consider the observation of the spectrum right after n=200 pulses.

Figure 3 provides the best representation of the spectral-resolution buildup from a single pulse to a pulse train. Since there is no interpulse interference with single pulses, we observe no variation in the excitation by single pulses as Δf_R is modified. As the number of pulses is increased, however, such interference becomes increasingly important for Δf_R values closer and closer to resonance. The measured resonance line becomes then progressively narrower, until it reaches the linewidth of the atomic line itself. As expected, this occurs once the number of pulses multiplied by T_R becomes larger than the atomic relaxation times. A direct experimental observation of such behavior can be found in Ref. [30].

The atomic linewidth Γ_a, then, can be directly obtained from the linewidth Γ_f of the peak in Fig. 3 noting that any variation in f_R need to be multiplied by the mode number in the comb in order to obtain the respective variation in the optical frequency of the mode. The two-photon transition $1 \rightarrow 7 \rightarrow 12$ corresponds to the transition $5S_{1/2}(F=2) \rightarrow 5P_{3/2}(F=3) \rightarrow 5D_{5/2}(F=4)$ at $\nu_{1,12} \simeq 770$ THz. Two modes N_1 and N_2 participate in the transition, one for its lower part (close to $5S_{1/2} \rightarrow 5P_{3/2}$) and the other for the upper transition (close to $5P_{3/2} \rightarrow 5D_{5/2}$). Since $f_R \approx 100$ MHz, we have $N_1+N_2=\nu_{1,12}/f_R \simeq 7.7 \times 10^6$. The full width at half maximum (FWFM) of the peak in Fig. 3 is $\Gamma_f \simeq 0.20$ Hz. In this way, the atomic linewidth is given by $\Gamma_a=(N_1+N_2)\Gamma_f \simeq 1.5$ MHz. This is larger, due to power broadening of the

atomic transition, than the radiative linewidth $\Gamma_{5D}=660$ kHz. The atomic pulse area for Figs. 2 and 3 is $\theta_a=0.01\pi$. In order to obtain $\Gamma_a \approx \Gamma_{5D}$, we should use $\theta \lesssim 10^{-3}\pi$. Remember that the atoms here are excited by trains of pulses, so that small pulse areas may lead to considerably larger atomic excitations than in the case of single pulses.

1. Spectrum

The narrowest curves in Fig. 3 clearly show some asymmetry on their wings. These come from other resonances on the same region of the scan. A complete scan of the spectrum, with a variation of 26 Hz in f_R, is given by the solid line in Fig. 4(a), plotting the population in $5D$ after $n=200$ pulses. From the discussion above, we note that a change in Δf_R on the order of $f_R/(N_1+N_2)\simeq 13$ Hz would be enough to repeat the two-photon spectra almost exactly, with just a different pair of modes being responsible for the resonant excitations. However, since the pulses are also resonant with the one-photon transitions from $5S$ to $5P$, which occur for resonant mode numbers on the order of $N_1 \simeq 3.8\times 10^6$, we observe an overall repetition of the spectrum only after Δf_R changes by $f_R/N_1 \simeq 26$ Hz. In this way, for each of the 26 Hz scans we discuss in the following, we will have a complete set of the one-photon resonances and two complete sets of the two-photon resonances.

The solid curve in Fig. 4(a) presents a clearly dominant peak due to the fact that, for the chosen f_0 and f_{ref}, we have simultaneous (for the same Δf_R) one- and two-photon resonances in the $1\rightarrow 7\rightarrow 12$ transition. This is a very strong, cycling transition in both $1\rightarrow 7$ and $7\rightarrow 12$ stages. A more common situation is shown in Fig. 4(b), where we chose $f_{ref}=100.12$ MHz, for which the one-photon $(1\rightarrow 7)$ and two-photon $(1\rightarrow 12)$ resonances do not occur simultaneously anymore for Δf_R varying from 0 to 26 Hz. In this case, as indicated in the figure, various two-photon resonances, between different states, occur with similar strengths. In Fig. 4(b) we identified only the most pronounced peaks, but we can already note the repetition of the two-photon resonances after 13 Hz, as expected from the above discussion.

The dominant peak in Fig. 4(a) helps to illustrate the effect that a change in f_0 would have in the spectrum. The dashed line in this figure presents the same scan as the solid line, but now with $f_0=40$ MHz. The peaks are then simply dislocated by a Δf_R such that $(N_1+N_2)\Delta f_R=2\Delta f_0$ and Δf_0 is the difference between the old and the new f_0. The factor 2 in this expression comes from the fact that two modes participate in the process, each carrying a unit of the f_0 dislocation. For the particular case of Fig. 4(a), we have $\Delta f_0=30$ MHz and $(N_1+N_2)\simeq 7.7\times 10^6$, with the corresponding dislocation of about 7.8 Hz in the spectrum.

The θ_a value employed in the above figures was chosen to be near commonly found experimental conditions for cw power of the pulse train [29]. It is possible, however, to obtain higher values for θ_a, and it would be important for the theory to model power regions as broad as possible. As we discussed before, the present theory works in principle at arbitrary perturbation orders, and we can then use a longer perturbation series to be able to work at higher excitation powers. For the calculations presented in this section, we used $m=12$ for the perturbation order. In this way, we were able to model the system well into the saturation region, as shown in Fig. 5, where the $5D$ population approaches a value on the order of the unit. This is interesting to demonstrate the versatility of our method. However, since we are here mainly concerned with its applications to spectroscopy, we will not explore this region of parameters, where the resonances get so broad that we loose information about the detailed structure of the spectrum.

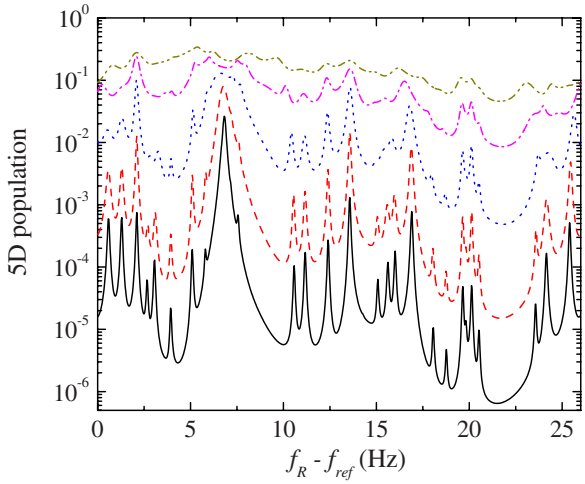

FIG. 5. (Color online) Population in level $5D$ as a function of f_R for various values of θ_a. From the lowest to the highest curve, we have θ_a values of 0.01π, 0.02π, 0.04π, 0.07π, 0.1π, respectively. The other relevant parameters are $f_{ref}=100$ MHz, $f_0=10$ MHz, and $n=200$.

2. Numerical errors

As discussed in the previous paragraph, we employed a $m=12$ perturbation-order calculation for the curves in Figs. 2–5. This value is determined from the minimization of errors in the program. Usually, computational time is the crucial problem in the calculation of such perturbation series. However, due to the efficient algorithm introduced in Sec. III, we ended up not being limited at all by that. This was the key element that enabled us to move toward considerably larger perturbation orders. Even though, we found a limitation in the accumulation of numerical round-up errors as the perturbation series increases.

In order to have a measure of such numerical errors, we introduce the quantity

$$\varepsilon = \left| 1 - \sum_i \rho_{ii} \right|, \tag{30}$$

where the label i run over all states in the system. This quantity, then, measures the depart from normalization of the density matrix after the system evolved by a certain amount of time $t_e=nT_R$. Note that, in the formal solution given above for the system of Bloch equations, we do not impose such normalization at every step. This normalization should come naturally as a result of the system's dynamics and the normalization of the initial state. In this way, imperfections in the modeling of this dynamics are reflected directly in the

normalization of the density matrix as the system evolves, which can then be used to quantify such imperfections.

For the various curves in Fig. 5, we can obtain the maximum error $\varepsilon_{\max}$ that occur in each 26 Hz scan of f_R. From its lowest θ_a (0.01π) to the highest (0.1π), we observe that $\varepsilon_{\max}$ grows from 10^{-14} up to 10^{-6}. For the parameters of that figure, we also observe that no matter how low we decrease θ_a or how high we make m, we always reach a plateau of 10^{-14} for $\varepsilon_{\max}$.

This behavior has actually a simple explanation. The final calculation of $\hat{\rho}(t)$ needs as input two files generated previously, the ones storing $\hat{M}$ and $\hat{U}_I^0$, respectively. These files, however, are presently generated and accessed using standard pre-formatted printing/reading functions that have a 17-decimal-digits limit for the stored numbers. This problem can be solved in a straightforward way by changing from text to binary printing/reading routines. However, for the scope of the present work, we found such error levels acceptable, and did not proceed with such modifications. Of course, these round up errors affect more the calculations once we start to increase θ_a, our perturbation parameter.

Finally, this source of numerical errors is still the dominant one when we consider the excitation by pulses with arbitrary shapes. In this way, the discussion above also applies to all situations treated in the following. Since we will keep $\theta_a=0.01\pi$ and $m=12$ from now on, our typical error level for the 26 Hz scans will be, in the following, the minimum $\varepsilon_{\max}\approx 10^{-14}$.

B. Hyperbolic-secant pulses

Now we will start discussing the case of excitation by trains of pulses with arbitrary pulse shapes. We begin by the simplest pulse shape found in experiments, the hyperbolic-secant pulse,

$$\mathcal{E}(t)=\mathcal{E}_0\,\mathrm{sech}(1.763t/T_p), \tag{31}$$

where T_p is the pulse temporal width. In order to compare with the previous results, we keep $\theta_a=0.01\pi$, $m=12$, $n=200$, and $f_0=10$ MHz from now on. We are also going to write the pulse field as a long vector (N elements) storing the real and imaginary parts of $\mathcal{E}(t_i)$ for times t_i evenly separated by Δt, $t_i=t_{i-1}+\Delta t$. Of course, this is not essential for such pulse shape since it has a simple analytical expression. However, this general description is important for the other pulse shapes considered in the next sections, particularly for 0π pulses, and we want to directly compare their results with the ones for sech pulses.

In the following, we consider sech pulses with different widths, 20 and 150 fs, two values commonly found in experiments. For the 150 fs pulse, we use a vector for the electric field with about 10^6 components and $\Delta t=10$ fs. For the 20 fs, the analogous vector has 4×10^6 and $\Delta t=2.5$ fs. These vector sizes were determined to provide more than enough spectral resolution to treat the 0π pulses [29,45,46].

The 26 Hz scan of f_R for these two pulse widths are shown in Figs. 6(a) and 6(b). In Fig. 6(a) the top curve shows again the result of Fig. 4(b) for the impulsive approximation, with a plot of the total population of level $5D$ as f_R is

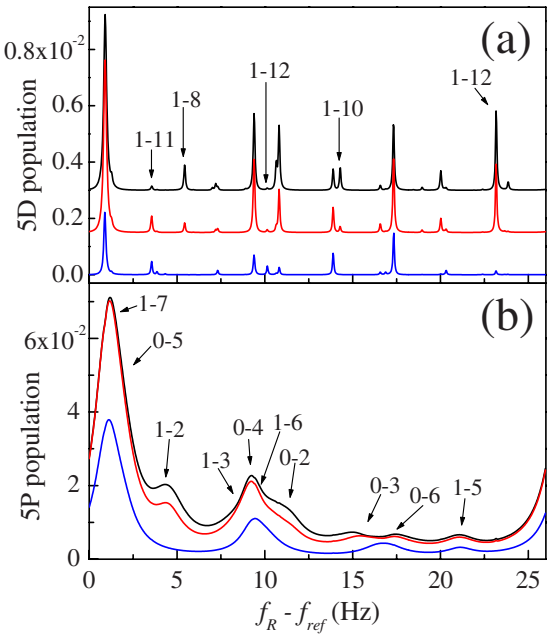

FIG. 6. (Color online) Population in levels (a) $5D$ and (b) $5P$ as a function of f_R for two different pulse widths and for the impulsive approximation. From the bottom to the top, we show the curves for $T_p=150$ fs, for $T_p=20$ fs, and for the impulsive approximation, respectively. In (a) we dislocated, for clarity, the vertical origin of the two upper curves. All other parameters are the same as for Fig. 4(b). The labels $(i-j)$ in each peak indicate the initial (i) and final (j) states of the respective resonances.

scanned starting at $f_{ref}=100.12$ MHz. The other two curves are, from top to bottom, the analogous curves for the pulses with $T_p=20$ fs and $T_p=150$ fs, respectively. In Fig. 6(b), we have the similar curves for the total population of level $5P$, where we also indicate the region of each single-photon resonance. Labels for various of the two-photon resonances in Fig. 6(a) are provided in Fig. 4(b). Even though, we still provide labels in Fig. 6(a) for five peaks whose variation with the pulse width we want to analyze in more detail.

The kind of problem we treat here, coherent dynamics of a multilevel system excited by a large number of frequency modes, involves always a large collection of different behaviors and physical effects, whose causes are not always clear from the calculation output. The modeling, however, allows one to investigate these effects from multiple angles, many of which are difficult to access experimentally. In the case we treat here, for example, it is straightforward to access the total population in level $5D$ (through the decay in the blue of level $6P$), but it is harder to access the populations in levels $5P$ and $5S$. It is even harder to have information on each separate hyperfine state. In this way, one may use the present calculation not only to predict different behaviors for the final signals, but also to help in their interpretation. This digression is just to point out that we do not aim here to give full explanation for all different features appearing in Fig. 6 and the other figures that follow in this article. There is a large complexity in each of them, so that we will highlight just a few of their features in order to keep our focus in the broad possibilities of application of the theory.

The first important feature to note in Fig. 6 is the overall decrease in the atomic excitation when we increase the pulse width from 20 to 150 fs, even though we kept θ_a constant. There was also a similar decrease, but in a small magnitude, when passing from the impulsive approximation to considering pulses with $T_p=20$ fs. One point that affects the curves directly is the fact that the laser bandwidth is changing from effectively infinity (impulsive approximation), to about 55 nm ($T_p=20$ fs), and then to 7 nm ($T_p=150$ fs). In this way, the 150 fs pulse has not enough bandwidth to excite the $5P_{1/2}$ states (labeled 2 and 3). All peaks involving these levels, then, disappear in Fig. 6(b) once T_p is changed to 150 fs. In Fig. 6(a), two peaks at least also disappear for this reason, the ones labeled 1:8 and 1:10. For the conditions of high bandwidth in Fig. 6(a), these peaks are actually a result of two sequential transitions, $1\rightarrow 2\rightarrow 8$ and $1\rightarrow 3\rightarrow 10$, respectively, which are greatly reduced once states 2 and 3 cease to be excited.

On the other hand, we also see a considerable decrease of peaks that continue to be close to resonance after changing to $T_p=150$ fs, like the one for the transition 1:7 in Fig. 6(b). To understand this point one has to remember the precise definition of θ_a in Eq. (21). This parameter gives an idea of the strength of a single-photon atomic excitation by a particular, well behaved pulse, if the pulse's central frequency is resonant to the atomic transition. However, if the pulse continue to be well behaved, but its central frequency is detuned from resonance, the effective pulse area θ_{ij} (the one that is directly related to the atomic-excitation strength of transition $i\rightarrow j$) is modified to take into account such detuning, being proportional to the spectrum component of the pulse at the detuned atomic resonance,

$$\theta_{ij}=\frac{2e\mu_{i,j}}{\hbar}\int_{-\infty}^{\infty}\mathcal{E}(t)e^{\Delta_{ij}t}dt,$$

with Δ_{ij} the detuning of the laser central frequency ω_L to the atomic transition frequency ω_{ij}. In this way, when we change the pulse bandwidth from 55 to 7 nm, we change the relative detuning of all atomic states from the laser central frequency, effectively decreasing the strength of all atomic single-photon transitions.

Note that this explains also the similar features observed in the passage from the impulsive approximation to the situation where $T_p=20$ fs. In this case, we move from a situation where all transitions were effectively on resonance, to a situation where level $5P_{1/2}$ presents some noticeable detuning, but level $5P_{3/2}$ can still be considered on resonance. Accordingly, we notice in Fig. 6(b) that the regions that are most affected by the change from impulsive approximation to the 20 fs pulses are the ones related to the one-photon transitions to states 2 and 3 of level $5P_{1/2}$.

The two-photon transitions on Fig. 6(a), on the other hand, present a more diverse behavior. Note, for example, that the peaks 1:11 at 3.56 Hz and 1:12 at 10.1 Hz both increase as we change from the impulsive approximation to considering pulses with $T_p=20$ fs. The 1:12 peak actually increases even further once we change T_p to 150 fs. This increase is a result of different population distributions among the two lowest-energy states, 0 and 1. Even though θ_a is small, in the long run the action of the pulse train can lead to large population redistributions in the ground level $5S_{1/2}$, due to optical pumping through levels $5P_{1/2}$ and $5P_{3/2}$. If, for example, there is a resonance between state 0 and a state in level $5P$, and at the same time there is no resonance involving state 1, the population will tend to accumulate in state 1. Of course, with the number of levels at play in Fig. 6, the picture here is more complicated, with competition between the optical pumping through different states in the first manifold.

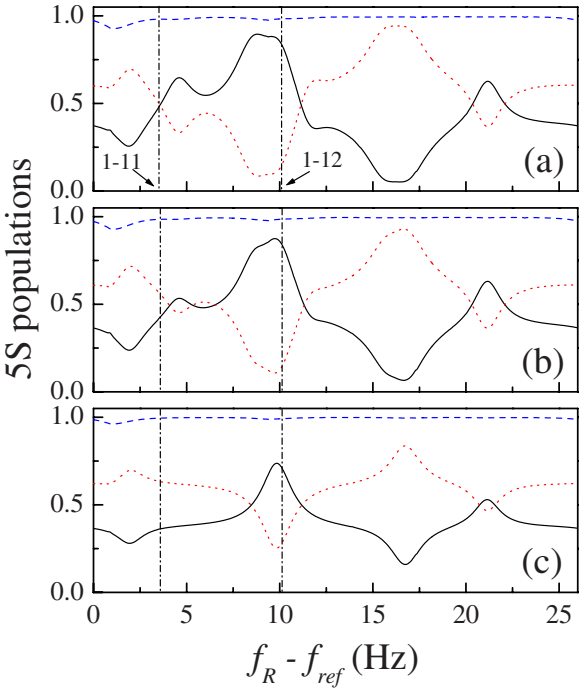

FIG. 7. (Color online) Populations in level $5S$ as a function of f_R for (a) impulsive approximation, (b) $T_p=20$ fs, and (c) $T_p=150$ fs. The dashed curve on the top of each frame is the total population in $5S$, and the solid and dotted lines are the results for the populations in states 0 and 1, respectively. The two vertical lines (dash-dotted) indicate the positions of the peaks 1:11 and 1:12. The other parameters are the same as for Fig. 4(b).

In Fig. 7 we show then the ground level populations as a function of f_R. We show the total population in $5S$ (dashed curve), as well as the populations in states 0 (solid curve) and 1 (dotted curve). The dips in the dashed curves reflect then the transfer of population to the excited states, and are directly related to the highest peaks in Figs. 6(a) and 6(b). In this way, we observe directly how the population distributions change in this level from the impulsive approximation to the cases with $T_p=20$ and 150 fs, respectively. The two vertical lines in each frame point to the positions of peaks 1:11 and 1:12. From these data, we observe that in 3.56 Hz (peak 1:11) the populations in states 0 and 1 are distributed 50:50 under the impulsive approximation, but this distribution changes to 43:57, favoring state 1, once we consider $T_p=20$ fs. This increase in state 1 population results then in a corresponding increase in the 1:11 peak. When we change to $T_p=150$ fs, the populations of states 0 and 1 are further redistributed to 36:64. In this case, however, we do not ob-

serve an absolute increase in the peak since the effective pulse area for the intermediate 1:7 transition also decreases when T_p changes to 150 fs, as discussed above. For 10.1 Hz (peak 1:12), we observe a similar trend, with a strong depletion of state 1 for the impulsive approximation and T_p =20 fs (85% of population in state 0) being attenuated when we move to T_p=150 fs (71% in state 0).

There is another 1:12 resonance at about 23 Hz. From Fig. 7, note that around 23 Hz there is no considerable change in the population distribution among states 0 and 1 in the three situations considered in Fig. 6. In this case, we see then that there is no change in the 1;12 peak when we pass from the impulsive approximation to T_p=20 fs. However, once we change to T_p=150 fs, we notice a considerable decrease of the peak due only to the modification of effective area of the pulse exciting the atom through the sequential transition 1 $\rightarrow$7$\rightarrow$12. The transition at 23 Hz is still affected by the wing of the 1:7 resonance occurring at about 26 Hz, and the modification of the single-photon transition strength (due to the larger relative detuning to the laser center frequency) affects both the red and blue parts of the sequential transition, at 780 nm (1:7) and 776 nm (7:12), respectively.

In order to have a broad understanding of Fig. 7, note that the balance between the populations in levels 0 and 1 depend on the prevailing one-photon resonance on that region of the spectrum. In Fig. 7(c), for example, we have only four possible transitions from the 5*S* manifold that contribute to the optical pumping between the two ground states: 0:5, 0:6, 1:5, and 1:6. The transitions 1:7 and 0:4 do not lead to optical pumping since the complementary transitions, 0:7 and 1:4, to the other ground state are forbidden. When comparing Figs. 6(b) and 7(c), we notice then that the resonances 1:5 and 1:6 lead to larger populations in 0, and the resonances 0:5 and 0:6 to larger populations in 1. Figures 7(a) and 7(b) become more complex with the increasing competition of the transitions through states 2 and 3 as the pulse becomes spectrally broader.

C. Chirped pulses

A frequency chirp on a femtosecond pulse implies that some frequency components of the pulse are arriving before others at a particular point in space. If the chirp is positive, the lower frequencies arrive sooner. On the other hand, a negative chirp results in the higher frequencies arriving sooner. The result in both cases is a longer, not-transform-limited pulse. This is one of the most common distortions a femtosecond pulse can present in its shape since it can acquire such chirp by passing through common optical components, like a thick beam splitter or a glass window. Of course, for the experiments we aim to model, we consider more controllable ways to introduce frequency chirps. By using a double pass grating stretcher and compressor [30,47], for example, it is possible to generate a tunable linear chirp in a femtosecond pulse, resulting in pulse shapes like the ones we consider in the following.

In the theory, the frequency chirp is introduced by first taking the fast Fourier transform (FFT) of the pulse envelope $\mathcal{E}'(t)$, obtaining in this way the pulse spectrum $\tilde{\mathcal{E}}(\Omega)$ around the laser center frequency ($\Omega=\omega-\omega_L$). The spectrum is then multiplied by a transfer function $F_{chirp}(\Omega)$ corresponding to the appropriate frequency chirp, resulting in the new spectrum $\tilde{\mathcal{E}}_{chirp}(\Omega)$,

$$\tilde{\mathcal{E}}_{chirp}(\Omega) = F_{chirp}(\Omega)\tilde{\mathcal{E}}(\Omega) = e^{i\phi''\Omega^2/2}\tilde{\mathcal{E}}(\Omega), \qquad (32)$$

where ϕ'' is the chirp parameter, the second-order derivative of the pulse phase with respect to its frequency, corresponding to a certain amount of group velocity dispersion (GVD). In order to calculate $\hat{U}_I^0(t)$, we then take the inverse fast Fourier transform (IFFT) of $\tilde{\mathcal{E}}_{chirp}(\Omega)$, obtaining the final distorted pulse envelope $\mathcal{E}'_{chirp}(t)$. Using this new pulse envelope, we proceed with the calculations as in the last section.

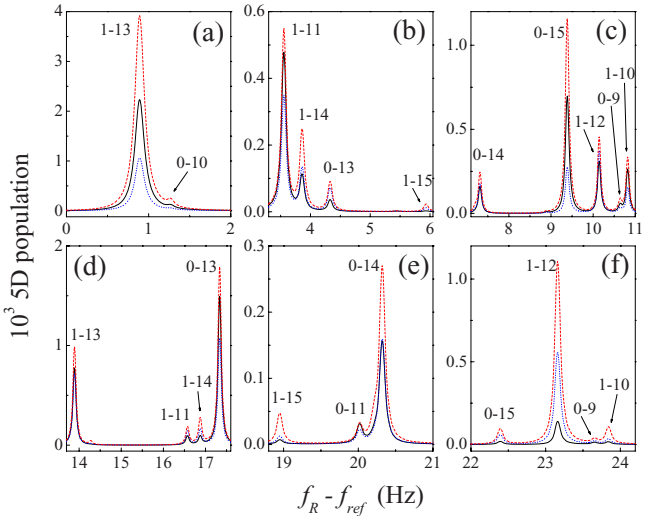

FIG. 8. (Color online) Population in level 5*D* as a function of f_R for three different values of the linear frequency chirp ϕ'': (dashed line) 33 750 fs^2, (solid line) 0, and (dotted line) −33 750 fs^2. For clarity, the 26 Hz interval corresponding to a complete scan was divided in six, consecutive frames with different vertical scales. The original temporal pulse width was T_p=150 fs. The other parameters are the same as for Fig. 4(b). The various peaks are identified in the same way as in the previous figures.

Figure 8 shows then how the 26 Hz spectrum of Fig. 6, with T_p=150 fs, is modified as some frequency chirp is introduced. The solid line in each frame of Fig. 8 represents the spectrum without chirp. The dashed line presents the same spectrum but now with a frequency chirp of ϕ'' =33750 fs^2. For the dotted line, we have ϕ''=−33750 fs^2. For clarity, we divided the 26 Hz spectrum in six frames, with different portions of it having different vertical scales. In this way, we can appreciate modifications on peaks of quite different sizes.

We concentrate on these few values of ϕ'' because we found this is enough to highlight some general aspects of the interaction of chirped pulses with the atomic system. The first point to note in Fig. 8 is that the dashed line is always on top of the other curves, i.e., for these values of ϕ'' the positive chirp always increase the population in 5*D*. We may have, however, any relation between the solid and dotted lines, and it will be useful to label the curves according to

which condition leads to a larger $5D$ population. We call then type A peaks the ones for which the solid line is on top of the dotted line, i.e., a negative chirp decreases the population in $5D$. Examples of type A peaks are the 1:13, 0:10, and 1:11 resonances up to 3.7 Hz; the 0:15, 0:9, 1:10, and 1:13 peaks between 9 and 14 Hz; the 0:13 peak at 17.3 Hz; and the 0:11 peak at 20 Hz. The type B peak, on the other hand, shows the opposite behavior, with the negative chirp increasing the $5D$ population when compared to a similar transform-limited pulse. Examples of type B peaks are the 1:14, 0:13, 1:15, and 0:14 peaks between 3.5 and 8 Hz; the 1:12 peak at 10.1 Hz; the 1:1, 1:4, and 1:5 resonances between 16 and 19 Hz; and the 0:14, 0:15, 1:12, 0:9, and 1:10 peaks between 20 and 24 Hz.

In order to understand this overall behavior, it is essential to remember that, in general, a transform-limited pulse is not the most efficient pulse shape to excite a two-photon transition that has an intermediate state in the middle of the pulse spectrum. This was first pointed out, to the best of our knowledge, by Dudovich *et al.* in Ref. [48]. There, the authors demonstrated that the two-photon transition probability has two portions, one representing the on-resonance contribution and another for the off-resonance contributions. The on-resonance portion is shifted by a $\pi/2$ phase with respect to the off-resonance portion, and the off-resonance spectral components below and above the intermediate resonance excite the system with a π phase difference between them. These phase differences result in destructive interference between different spectral components of the pulse contributing to the atomic excitation. In Ref. [48], the authors used spectral masks to modify the pulse spectrum to compensate for those phase differences, obtaining considerably stronger two-photon excitations than with the unmodified, transform-limited pulses.

Reference [48] considered the excitation of an atomic vapor by single pulses and not by phase-stabilized pulse trains. In this way, the on-resonance and off-resonance components on that work always appear together. When considering cold atoms excited by femtosecond frequency combs, on the other hand, it is possible to tune the different modes on and out of resonance and we can actually single out two-photon excitations which has strong on-resonance components (sequential transitions) and others that are almost purely off-resonant two-photon transitions. Basically, when crossing the information of Figs. 6(b) and 8, we observe that the type A peaks discussed above are all related to on resonance, sequential transitions. Note the coincidence of the 1:7, 0:5, 0:4, 1:6, 0:6, and 1:5 transitions in Fig. 6(b) with the type A peaks in Fig. 8. The spectral regions far from $5S \rightarrow 5P$ resonances are the ones presenting type B peaks. Note also the type B peak corresponding to the 1:12 transition around 10.1 Hz. That is a spectral region dominated by type A peaks, since we have both the 0:4 and 1:6 single-photon transitions occurring nearby. However, none of these two single-photon transitions are intermediate steps to the two-photon 1:12 transition, see Fig. 1, which is then very much off resonance from any relevant intermediate level.

For the sequential, type A transitions, a positive chirp enhance the two-photon excitation probability because the first portion ($5S \rightarrow 5P$ at 780 nm) of the sequential transition has smaller frequency than the second portion ($5P \rightarrow 5D$ at 776 nm). A negative chirp cause the opposite effect for the same reason, i.e., we try to excite the second transition prior to the first one. Note, however, that this enhancement and suppression of a sequential excitation by a pulse train occurs with much smaller intensity than what would be observed in single pulse excitations, since the atom is not at its ground state prior to each pulse in the train [30]. The type A peaks are dominated by this stepwise process, and the destructive interference between different off-resonance components do not play the major role here.

For type B peaks, however, we have a strong suppression of the on-resonance processes. These peaks are then a direct result of the combination between the red and blue part of the pulse spectrum to have a two-photon off-resonant transition. Thus, they are very sensitive to the destructive interference due to the π phase between the spectral components below and above the intermediate transition. A transform-limited pulse should suffer, then, a considerable suppression of its excitation due to such phase difference, and any perturbation of this relative phase may enhance the two-photon excitation probability with respect to a transform-limited pulse. In this way, we see both positive and negative chirp enhancing the $5D$ population when compared to an unchirped hyperbolic-secant pulse. The positive chirp still enhances more the excitation than the negative chirp for the reasons discussed in the previous paragraph.

D. 0π pulses

The resonant propagation of a weak ultrashort pulse through a dense sample of narrowband two-level atoms typically results in the distortion of the pulse envelope to a shape known as 0π pulse [37]. This is just a limit of the well-known area theorem [49], which, among other things, requires the area of a weak pulse to go to zero after propagation through a resonant two-level sample [50]. However, in the case where the pulse bandwidth is much larger than the bandwidth of the medium, this cannot absorb a large amount of the pulse energy. In this case, the pulse keeps a finite total energy, but develops an oscillatory tails that, after integration of the whole pulse envelope, leads to a zero pulse area.

It is possible to generate such 0π pulses by simply passing a weak femtosecond pulse through a heated vapor cell [51]. Examples of generation of 0π pulses from rubidium vapor cells can be found in the works of various groups [45,52,53]. Here we are interested in modeling the action of such a pulse over atoms stored in a magneto-optical trap. In this way, we consider that the 0π pulse was obtained by the propagation through a heated vapor cell prior to the action over the atoms. The heated cell then works here as a spectral mask applied to the pulse.

The introduction of such spectral mask in the theory is carried out in the same way as for the frequency-chirp mask. The difference is just the corresponding transfer function, which is now

$$F_{0\pi}(\Omega) = \exp[-A(\Omega)z], \tag{33}$$

where z is the distance propagated in the vapor cell and

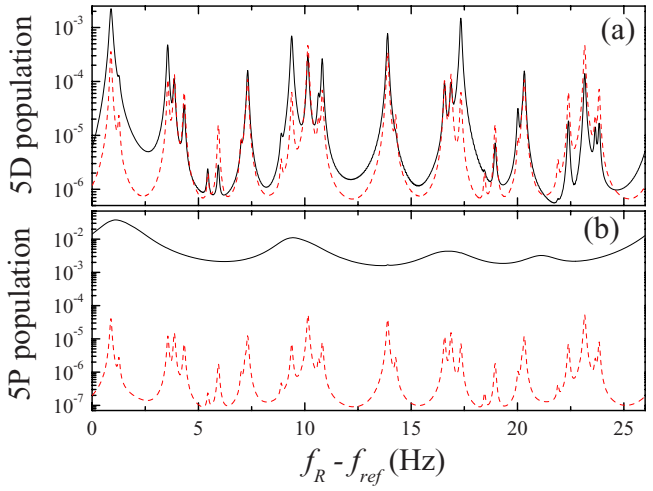

FIG. 9. (Color online) Populations in levels (a) $5D$ and (b) $5P$ as a function of f_R for two pulse shapes: hyperbolic secant (solid line) and 0π (dashed line). The hyperbolic-secant pulse has $T_p=150$ fs. The 0π pulse is generated from a 150 fs sech pulse, after propagation through a 5 cm long vapor cell with an atomic density corresponding to $\alpha_0=0.12$. The other parameters are the same as in Fig. 6.

$$A(\Omega) = \sum_i \alpha_i \int_{-\infty}^{\infty} \frac{g_i(\Delta)d\Delta}{1/T_2 + i(\Delta - \Omega)} \tag{34}$$

is the function describing both the dispersion and absorption of the pulse by the atomic medium [37,52]. In $A(\Omega)$, the sum runs over all $5S \rightarrow 5P$ transitions, $g_i(\Delta)$ gives the Doppler distribution of transition frequencies in the medium corresponding to the ith transition, and T_2 is the homogeneous transverse relaxation time of the medium. The parameter α_i is proportional to the atomic density of the medium and the square of the transition's dipole moment μ_i. When multiplied by z and the medium bandwidth, α_i gives the optical depth of the medium related to the ith transition [37]. Defining μ^2 as the sum of all μ_i^2, it is more convenient to specify the atomic optical density through a related parameter $\alpha_0=\alpha_i\mu^2/\mu_i^2$, the same for all transitions. In the following we consider T_2 as coming only from radiative decay, and the heated medium inhomogeneous broadening as $\gamma_I \simeq 1$ GHz.

Our interest here in this particular pulse shape has two reasons. First, it is the result of a high resolution mask, with resolution on the order of the atomic transition lines [53]. Second, it is straightforward to be obtained experimentally. In this way, we can test the theory we present here in a setup that highlights its application for finely shaped pulses, at the same time that can be readily addressed experimentally.

In Fig. 9 we show then the results for the 26 Hz scan of f_R with 0π and sech pulses, respectively. In frame (a) we have the results for the $5D$ population, and in (b) the results for level $5P$. The solid line, corresponding to a 150 fs sech pulse, is generated for the same parameters as in Fig. 6. The dashed line shows the similar results for the excitation by a train of 0π pulses generated from an original 150 fs sech pulse, after its propagation through 5 cm of a vapor cell with $\alpha_0=0.12$. These parameters were found to model well the generation of 0π pulses under common conditions in our group [29,45,46].

The first and most characteristic feature of the excitation by 0π pulses is shown in Fig. 9(b): the almost complete suppression of excitation of the single-photon transition, the $5P$ level. When the excitation pulse changes from sech to 0π, the spectrum of level $5P$ in Fig. 9(b) starts to follow the one at level $5D$, since it results mainly from the decay from these upper states. This behavior was already discussed in Ref. [29], for the case of a simpler, three-level model of the atom.

For level $5D$, the behavior shown in Fig. 9 follows closely the discussion of last section, with distinct behaviors for sequential transitions (type A peaks) and pure two-photon transitions (type B peaks). As expected from the suppression of excitation to $5P$, the sequential transitions are strongly suppressed. The purely two-photon transitions, on the other hand, may be even enhanced, since the spectral dispersion on the 0π pulse disturbs some of the two-photon destructive interferences characteristic of transform-limited pulses (see previous section). As examples of this behavior, we have the set of peaks from 21 to 25 Hz in Fig. 9.

This enhancement of the $5D$ excitation by 0π pulses, however, is a feature that strongly depends on the atomic density. Typically, we observe such behavior for moderate values of α_0, like the one in Fig. 9, when the 0π pulse starts to appear. In this situation, we notice a complete depletion of the pulse's spectral components corresponding to each single-photon transition [52], but this depletion is very sharp around the Doppler-broadened atomic resonances. As α_0 is increased, such depletion extends over a larger portion of the pulse spectrum. The two-photon transition is then increasingly affected by this disappearance of spectral components around the single-photon resonances. Eventually, for high enough values of α_0, the whole $5D$ spectrum excited by the train of 0π pulses will have smaller values than the one excited by the corresponding sech pulses.

V. CONCLUSIONS

In this work we introduced a theory to model the interaction between a train of ultrashort pulses and a multilevel atom. We considered a well-stabilized pulse train, with both its repetition frequency and interpulse phase locked to some frequency standard, a light field usually referred to as a frequency comb. The pulses in the train can have here an arbitrary shape, modified by spectral masks with resolutions up to a few comb lines. Even though it is a perturbative theory, it was setup to work at an arbitrary perturbation order. Specifically, all results presented here were obtained with a twelfth order perturbation series, which effectively allowed us to investigate even highly saturated regimes. In this way, this theory is able to model a large class of experimental conditions, and to serve as a tool to guide complex experiments trying to merge spectral resolution with the coherent control of atomic transitions.

In order to demonstrate the versatility of our treatment, we modeled the interaction of rubidium atoms with trains of pulses of three different shapes: hyperbolic secant, hyper-

bolic secant with frequency chirp, and 0π. More specifically, we modeled the two-photon excitation from $5S$ to $5D$ in ^{87}Rb, involving 16 different hyperfine states, with the center of the frequency comb tuned to the two-photon resonance, at 778 nm. Throughout the analysis of our results, we showed the strong dependence of the relative strength of the spectral lines with the pulse shape. In this way, we highlighted the possible applications that coherent-control techniques may have in direct frequency-comb spectroscopy, by magnifying different spectral components in a controllable way. Conversely, our results can also be understood as indicating the possible applications of frequency combs to coherent control, by using the spectral resolution of the comb to select different atomic-excitation outputs.

We designed the present theory to model directly feasible experiments in cold atoms. A first stage of comparison between its results and actually experiments was already carried out in Refs. [6,44]. In these previous experimental works, comparison was made with a preliminary version of this theory, employing a fourth-order perturbation series and the impulsive approximation. As a result, such theory was established as a proper guide to experiments, even in its simplified version employed in Refs. [6,44]. We understand that the next step now is the comparison of the present theory with experiments in which the pulse shape is changed in a controllable way, i.e., the comparison with situations like the ones modeled in Secs. IV B–IV D of this paper. We hope, then, the present treatment may foster experimental activity along these lines, contributing to develop the engineering of atomic-state control by frequency combs.

ACKNOWLEDGMENTS

This work was largely motivated by a series of experiments at Jun Ye's group. D.F. acknowledges then the many discussions with Jun Ye and his students at the time, Adela Marian and Matthew Stowe. The authors acknowledge also fruitful discussions with Sandra Vianna and Lucio Acioli. This work was supported by CNPq, FACEPE, and CAPES (Brazilian Agencies).

[1] Th. Udem, R. Holzwarth, and T. W. Hansch, Nature (London) **416**, 233 (2002).
[2] J. Ye and S. T. Cundiff, *Femtosecond Optical Frequency Comb Technology, Principle, Operation and Application* (Springer, New York, USA, 2005).
[3] J. L. Hall, Rev. Mod. Phys. **78**, 1279 (2006).
[4] T. W. Hansch, Rev. Mod. Phys. **78**, 1297 (2006).
[5] M. C. Stowe, M. J. Thorpe, A. Pe'er, J. Ye, J. E. Stalnaker, V. Gerginov, and S. A. Diddams, Adv. At., Mol., Opt. Phys. **55**, 1 (2008).
[6] A. Marian, M. Stowe, J. Lawall, D. Felinto, and J. Ye, Science **306**, 2063 (2004).
[7] M. J. Thorpe, K. D. Moll, R. J. Jones, B. Safdi, and J. Ye, Science **311**, 1595 (2006).
[8] M. J. Thorpe, D. Balslev-Clausen, M. S. Kirchner, and J. Ye, Opt. Express **16**, 2387 (2008).
[9] S. Witte, R. Th. Zinkstok, W. Ubachs, W. Hogervorst, and K. S. E. Eikema, Science **307**, 400 (2005).
[10] C. Gohle, T. Udem, M. Herrmann, J. Rauschenberger, R. Holzwarth, H. A. Schuessler, F. Krausz, and T. W. Hansch, Nature (London) **436**, 234 (2005).
[11] R. Teets, J. N. Eckstein, and T. W. Hansch, Phys. Rev. Lett. **38**, 760 (1977).
[12] M. M. Salour, Rev. Mod. Phys. **50**, 667 (1978).
[13] J. N. Eckstein, A. I. Ferguson, and T. W. Hansch, Phys. Rev. Lett. **40**, 847 (1978).
[14] A. I. Ferguson, J. N. Eckstein, and T. W. Hansch, Appl. Phys. (Berlin) **18**, 257 (1979).
[15] B. Couillaud, A. Ducasse, L. Sarger, and D. Boscher, Appl. Phys. Lett. **36**, 407 (1980).
[16] J. Mlynek, W. Lange, H. Harde, and H. Burggraf, Phys. Rev. A **24**, 1099 (1981).
[17] Y. Fukuda, J. Hayashi, K. Kondo, and T. Hashi, Opt. Commun. **38**, 357 (1981).
[18] E. Krüger, J. Opt. Soc. Am. B **12**, 15 (1995).
[19] M. J. Snadden, A. S. Bell, E. Riis, and A. I. Ferguson, Opt. Commun. **125**, 70 (1996).
[20] M. A. Newbold and G. J. Salamo, Phys. Rev. A **22**, 2098 (1980).
[21] G. F. Thomas, Phys. Rev. A **35**, 5060 (1987).
[22] P. W. Milonni and L. E. Thode, Appl. Opt. **31**, 785 (1992).
[23] L. C. Bradley, J. Opt. Soc. Am. B **9**, 1931 (1992).
[24] A. Gavrielides and P. Peterson, Opt. Commun. **104**, 46 (1993).
[25] R. J. Temkin, J. Opt. Soc. Am. B **10**, 830 (1993).
[26] E. Krüger, Z. Phys. D: At., Mol. Clusters **31**, 13 (1994).
[27] N. V. Vitanov and P. L. Knight, Phys. Rev. A **52**, 2245 (1995).
[28] A. A. Soares and L. E. E. de Araujo, Phys. Rev. A **76**, 043818 (2007).
[29] D. Felinto, L. H. Acioli, and S. S. Vianna, Phys. Rev. A **70**, 043403 (2004).
[30] M. C. Stowe, F. C. Cruz, A. Marian, and Jun Ye, Phys. Rev. Lett. **96**, 153001 (2006).
[31] M. C. Stowe, A. Pe'er, and J. Ye, Phys. Rev. Lett. **100**, 203001 (2008).
[32] J. Ye, Nat. Photonics **1**, 447 (2007).
[33] D. Sofikitis, S. Weber, A. Fioretti, R. Horchani, M. Allegrini, B. Chatel, D. Comparat, and P. Pillet, New J. Phys. **11**, 055037 (2009).
[34] M. P. A. Branderhorst, P. Londero, P. Wasylczyk, C. Brif, R. L. Kosut, H. Rabitz, and I. A. Walmsley, Science **320**, 638 (2008).
[35] F. Weise and A. Lindinger, Opt. Lett. **34**, 1258 (2009).
[36] W. H. Press, S. A. Teukolsky, W. T. Vetterling, and B. P. Flannery, *Numerical Recipes in C: The Art of Scientific Computing* (Cambridge University Press, Cambridge, England, 1999).
[37] M. D. Crisp, Phys. Rev. A **1**, 1604 (1970).
[38] F. Nez, F. Biraben, R. Felder, and Y. Millerioux, Opt. Commun. **102**, 432 (1993).
[39] J. Ye, S. Swartz, P. Jungner, and J. L. Hall, Opt. Lett. **21**, 1280 (1996).

[40] G. P. Barwood, P. Gill, and W. R. C. Rowley, Appl. Phys. B: Photophys. Laser Chem. **53**, 142 (1991).
[41] D. Felinto, C. A. C. Bosco, L. H. Acioli, and S. S. Vianna, Opt. Commun. **215**, 69 (2003).
[42] D. Aumiler, T. Ban, H. Skenderovic, and G. Pichler, Phys. Rev. Lett. **95**, 233001 (2005).
[43] T. Ban, D. Aumiler, H. Skenderovic, S. Vdovic, N. Vujicic, and G. Pichler, Phys. Rev. A **76**, 043410 (2007).
[44] A. Marian, M. C. Stowe, D. Felinto, and J. Ye, Phys. Rev. Lett. **95**, 023001 (2005).
[45] D. Felinto, L. H. Acioli, and S. S. Vianna, Opt. Lett. **25**, 917 (2000).
[46] D. Felinto, C. A. C. Bosco, L. H. Acioli, and S. S. Vianna, Phys. Rev. A **64**, 063413 (2001).
[47] O. E. Martinez, IEEE J. Quantum Electron. **23**, 59 (1987).
[48] N. Dudovich, B. Dayan, S. M. Gallagher Faeder, and Y. Silberberg, Phys. Rev. Lett. **86**, 47 (2001).
[49] S. L. McCall and E. L. Hahn, Phys. Rev. Lett. **18**, 908 (1967).
[50] L. Allen and J. Eberly, *Optical Resonance and Two-Level Atoms* (Dover, New York, 1987).
[51] J. E. Rothenberg, D. Grischkowsky, and A. C. Balant, Phys. Rev. Lett. **53**, 552 (1984).
[52] U. Kallmann, S. Brattke, and W. Hartmann, Phys. Rev. A **59**, 814 (1999).
[53] N. Dudovich, D. Oron, and Y. Silberberg, Phys. Rev. Lett. **88**, 123004 (2002).